

# Reproducing cosmic evolution of galaxy population from $z = 4$ to 0

Takashi OKAMOTO<sup>1</sup>

<sup>1</sup>*Department of Cosmosciences, Graduates School of Science, Hokkaido University, N10 W8, Kitaku, Sapporo, 060-0810, Japan  
okamoto@astro1.sci.hokudai.ac.jp*

Ikkoh SHIMIZU<sup>2</sup>

<sup>2</sup>*Department of Astronomy, School of Science, The University of Tokyo, 7-3-1 Hongo, Bunkyo-ku, Tokyo 113-0033  
shimizu@astron.s.u-tokyo.ac.jp*

and

Naoki YOSHIDA<sup>3,4</sup>

<sup>3</sup>*Department of Physics, The University of Tokyo, 7-3-1 Hongo, Bunkyo-ku, Tokyo 113-0033, Japan*

<sup>4</sup>*Kavli Institute for the Physics and Mathematics of the Universe, TODIAS, The University of Tokyo, 5-1-5 Kashiwanoha, Kashiwa, Chiba 277-8583, Japan  
naoki.yoshida@phys.s.u-tokyo.ac.jp*

(Received ; accepted )

## Abstract

We present cosmological hydrodynamic simulations performed to study evolution of galaxy population. The simulations follow timed release of mass, energy, and metals by stellar evolution and employ phenomenological treatments of supernova feedback, pre-supernova feedback modeled as feedback by radiation pressure from massive stars, and quenching of gas cooling in large halos. We construct the fiducial model so that it reproduces the observationally estimated galaxy stellar mass functions and the relationships between the galaxy stellar mass and the host halo mass from  $z = 4$  to 0. We find that the fiducial model constructed this way naturally explains the cosmic star formation history, the galaxy downsizing, and the star formation rate and metallicity of the star-forming galaxies. The simulations without the quenching of the gas cooling in large halos overproduce massive galaxies at  $z < 2$  and fail to reproduce galaxy downsizing. The simulations that do not employ the radiation pressure feedback from young stars predict too strong redshift evolution of the mass-metallicity relation. Furthermore, the slope of the relation becomes too steep at low redshift without the radiation pressure feedback. The metallicity dependence in the radiation pressure feedback is a key to explain the observed mass-metallicity relation. These facts indicate that these two processes in addition to supernova feedback are essential for galaxy evolution. Our simple phenomenological model is suitable to construct a mock galaxy sample to study physical properties of observed galaxy populations.

**Key words:** cosmology: theory – galaxies: formation – galaxies: evolution – methods: numerical

## 1. Introduction

Understanding galaxy formation is a challenging problem whose solution will require a concerted approach combining observational and theoretical work. There have been substantial advances on both fronts in the past decades. Numerical simulations are a powerful theoretical tool to study cosmic structure formation.  $N$ -body simulations are now able to predict non-linear growth of the dark matter-dominated density perturbations in great detail (Springel et al. 2005; Springel et al. 2008; Diemand et al. 2008; Boylan-Kolchin et al. 2009). Consequently, gravitational assembly of structure in a  $\Lambda$ -dominated Cold Dark Matter ( $\Lambda$ CDM) Universe is well understood and mostly consistent with observations. In order to make a direct comparison with observations, simulations must involve luminous matters (baryons) besides dark matter and dark energy. While semi-analytic models (e.g. White & Frenk 1991; Kauffmann et al. 1993; Somerville & Primack 1999; Cole et al. 2000; Okamoto & Nagashima 2003; Nagashima

et al. 2005) can paint galaxies onto dark matter distribution, hydrodynamic simulations can directly explore evolution of the galaxy population and the intergalactic medium (IGM) simultaneously and self-consistently (e.g. Katz et al. 1992; Weinberg et al. 1997; Kereš et al. 2005; Oppenheimer & Davé 2006; Ocvirk et al. 2008; Crain et al. 2009; Schaye et al. 2010; Vogelsberger et al. 2013). The baryonic processes that are essential for galaxy formation, such as gas cooling, star formation, and stellar and active galactic nuclei (AGN) feedback, constitute a complicated and highly non-linear network. Modeling them appropriately in hydrodynamic simulations is hence the major challenge for the theoretical studies of galaxy formation (see Okamoto et al. 2005; Scannapieco et al. 2012).

Some recent simulations successfully produce realistic galaxies (Okamoto et al. 2010; Governato et al. 2010; Guedes et al. 2011; Okamoto 2013; Stinson et al. 2013; Marinacci et al. 2013). The key ingredient is undoubtedly stellar feedback such as supernova (SN) feedback that ejects gas from galaxies to prevent too efficient

star formation. While it is possible to drive winds by resolving the detailed structure of the interstellar medium (ISM) in very high resolution simulations (Hopkins et al. 2012a), most of cosmological simulations invoke phenomenological treatments of feedback because of limited numerical resolution. Some studies employ explicit winds, either hydrodynamically decoupled (Springel & Hernquist 2003) or coupled (Dalla Vecchia & Schaye 2008). The wind properties may depend on the galaxy properties (Oppenheimer & Davé 2006; Okamoto et al. 2010). Other popular way of implementing effective feedback is injecting thermal energy into the ISM and then shutting off cooling of heated gas for a while (Thacker & Couchman 2001; Stinson et al. 2006; Stinson et al. 2013). Adding the feedback energy as non-thermal energy (e.g. turbulence) which decays in time-scale much longer than the cooling time has a similar effect (Teyssier et al. 2013).

We have applied the feedback model developed by Okamoto et al. (2008b) to large scale simulations to study high redshift galaxy populations, such as Lyman- $\alpha$  emitters (Shimizu et al. 2011), sub-mm galaxies (Shimizu et al. 2012), and Lyman break galaxies at  $z > 7$  (Shimizu et al. 2013; Inoue et al. 2014). While these simulations reproduce many observed properties of high redshift galaxies, our studies utilizing the large scale simulations have been limited to high redshift because too massive galaxies form at low redshift (see Shimizu et al. 2012). We also note that too many stars form in low mass halos at high redshift if we normalize the model to reproduce the luminosity (or stellar mass) function of the local faint galaxies (Moster et al. 2013; Okamoto 2013).

The first problem is well-known; stellar feedback alone cannot prevent monster galaxies from forming and hence we need a physical process that operates preferentially in large halos to quench gas cooling there (e.g. Benson et al. 2003). The top candidate of such a process is so-called AGN *radio mode* feedback (Croton et al. 2006; Bower et al. 2006). Sijacki et al. (2007) and Okamoto et al. (2008b) suggest that this radio mode feedback is naturally realized by considering the change of the accretion modes onto a supermassive blackhole. In fact, simulations including this feedback roughly reproduce galaxy stellar mass functions and stellar mass to halo mass relations for massive galaxies (Vogelsberger et al. 2013; Torrey et al. 2013).

A remedy for the second problem has been recently identified by Stinson et al. (2013); feedback prior to an SN, such as stellar winds and radiation from massive stars, is needed to match stellar mass-halo mass relations over a wide redshift range (Stinson et al. 2013; Kannan et al. 2013; Aumer et al. 2013).

The aim of this paper is to update our galaxy formation model originally developed by Okamoto et al. (2008b) and Okamoto et al. (2010) by adding several new feedback processes so that we can apply it for studies of galaxy population over wider mass and redshift ranges. We test our models against various observations and reveal roles of each feedback process to present a fiducial model.

The paper is organized as follows. In section 2, we describe our simulations and provide descriptions of our

modeling of baryonic processes. We present our results at  $0 \leq z \leq 4$  and compare them with the available observational estimates in section 3. We investigate resolution effects in section 4. Finally, we summarize our results and discuss future applications of the new model in section 5.

## 2. Simulations

We first describe our cosmological hydrodynamic simulations. The simulation code is based on an early version of Tree-PM smoothed particle hydrodynamics (SPH) code GADGET-3 which is a successor of Tree-PM SPH code GADGET-2 (Springel 2005). We have implemented a time-step limiter (Saitoh & Makino 2009) that reduces the time-step of a gas particle if it is too long compared to the neighboring gas particles. We have also added an artificial conductivity (Rosswog & Price 2007; Price 2008), in order to capture the instabilities at contact surfaces (see also Kawata et al. 2013), which cannot be captured by the standard SPH (Okamoto et al. 2003; Agertz et al. 2007), together with the time dependent artificial viscosity (Morris & Monaghan 1997).

We assume  $\Lambda$ CDM cosmology with the following parameters:  $\Omega_0 = 0.318$ ,  $\Omega_\Lambda = 0.682$ ,  $\Omega_b = 0.049$ ,  $\sigma_8 = 0.835$ ,  $n_s = 0.962$ , and a Hubble constant of  $H_0 = 100 h \text{ km s}^{-1} \text{ Mpc}^{-1}$ , where  $h = 0.67$ . These parameters are consistent with Planck 2013 results (Planck Collaboration 2013). Throughout this paper, we use a cosmological periodic box of the side length of  $40 h^{-1} \text{ Mpc}$  and start simulations from  $z = 127$  unless otherwise stated. We employ  $256^3$  dark matter particles and the same number of SPH particles. The total number the particles can change owing to the star formation. The mass of a dark matter particle is  $2.9 \times 10^8 h^{-1} M_\odot$  and that of an SPH particle is  $5.2 \times 10^7 h^{-1} M_\odot$ . The gravitational softening length is set to  $8.6 h^{-1} \text{ kpc}$  in comoving units both for the dark matter and SPH particles (and stars) until  $z = 3$ ; thereafter, it is frozen in physical units at the value,  $2.2 h^{-1} \text{ kpc}$ .

### 2.1. Baryonic processes

The simulations include many physical processes that are relevant to galaxy formation. Both photo-heating by a spatially uniform, time-evolving ultra-violet background and radiative cooling depend on gas metallicity as described in Wiersma et al. (2009a). The cooling and heating rates are computed individually for eleven elements (H, He, C, N, O, Ne, Mg, Si, S, Ca, and Fe). We track only nine elements and we take S and Ca to be proportional to Si (Wiersma et al. 2009b). As in Okamoto et al. (2005), we use the smoothed metallicity instead of the particle metallicity to compute the photo-heating and radiative cooling rates and to give the initial amount of each individual chemical element to newly born stars. Note however that we do not include explicit metal diffusion.

We assume star formation takes place when gas density exceeds a threshold density for star formation ( $n_H > n_{H,th} = 0.1 \text{ cc}^{-1}$ ), gas temperature is sufficiently low ( $T < T_{th} = 15000 \text{ K}$ ), and flows are converging ( $\nabla \cdot \mathbf{v} < 0$ ).

While, in our previous studies, we have treated a star forming gas particle as a hybrid particle that contains hot and cold phases (Okamoto et al. 2008b; Okamoto et al. 2010; Shimizu et al. 2011; Shimizu et al. 2012; Shimizu et al. 2013), we abandon doing this in this paper since global star formation properties of simulated galaxies are highly self-regulated by strong feedback and are almost independent of the treatment of the equation of states of the star-forming gas (Okamoto et al. 2010; Schaye et al. 2010).

The star formation rate (SFR) density,  $\dot{\rho}_*$ , for a gas particle with the density,  $\rho$ , is then simply given by

$$\dot{\rho}_* = c_* \frac{\rho}{t_{\text{dyn}}}, \quad (1)$$

where  $c_*$  and  $t_{\text{dyn}}$  are respectively the dimensionless star formation efficiency parameter and the local dynamical time. This formula corresponds to the Schmidt law that implies an SFR density proportional to  $\rho^{1.5}$ . We set  $c_* = 0.01$  in order to reproduce the observed relation between the surface gas density and the surface star formation rate density (Kennicutt 1998). Technically, we compute the probability,  $\mathcal{P}_*$ , for an SPH particle with which it spawns a new star particle of mass,  $m_*$ , during a time-step,  $\Delta t$ , as

$$\mathcal{P}_* = \frac{m_{\text{SPH}}}{m_*} \left[ 1 - \exp\left(-\frac{\Delta t}{t_*}\right) \right], \quad (2)$$

where  $m_{\text{SPH}}$  is the mass of the gas particle and the star formation time-scale  $t_*$  is defined as  $t_* = t_{\text{dyn}}/c_*$ . We use  $m_* = m_{\text{SPH}}^{\text{orig}}/2$  throughout this paper, where  $m_{\text{SPH}}^{\text{orig}}$  denotes the original SPH particle mass.

Stellar evolution is modeled as in Okamoto et al. (2010). We employ the Chabrier initial mass function (IMF: Chabrier 2003) and we use metallicity dependent stellar lifetimes and chemical yields (Portinari et al. 1998; Marigo 2001). The production of metals by SNe and AGB stars, stellar mass loss, and stellar feedback all take place on the time-scale dictated by stellar evolution considerations. When we compare our results with observational estimates that assume different IMFs, we convert them to the Chabrier IMF<sup>1</sup>.

We now discuss the numerical implementation of important *subgrid* processes included in our simulations.

## 2.2. Stellar feedback

In our subgrid model, stellar feedback gives rise to a wind by imparting kinetic energy and momentum to nearby gas particles. The wind is characterized by its initial speed,  $v_w$ .

The direction of the wind is chosen at random to be either parallel or antiparallel to the vector  $(\mathbf{v} - \bar{\mathbf{v}}) \times \mathbf{a}_{\text{grav}}$ , where  $\bar{\mathbf{v}}$  is the average velocity of the neighboring 64 dark matter particles and  $\mathbf{a}_{\text{grav}}$  is the gravitational acceleration. Okamoto et al. (2010) found that the direction of

the wind particle velocity defined in this way leads to wind particles being ejected preferentially along the rotation axis of a spinning object, and thus generating an ‘axial’ wind (Springel & Hernquist 2003). We assume that the newly launched wind particles are decoupled from hydrodynamic interactions for a brief period of time (Springel & Hernquist 2003). Full hydrodynamic interactions are enabled once a wind particle leaves the star-forming region ( $n_H < 0.01 \text{ cc}^{-1}$ ) or after the time,  $(10 \text{ kpc})/v_w$ , has elapsed, whichever occurs earlier.

### 2.2.1. Supernova-driven winds

We assume that some fraction of the energy released from SNe is potentially available to power the kinetic energy of the wind. Each SN releases energy of  $10^{51}$  erg and the fraction of energy used to drive wind is controlled by an efficiency parameter,  $\eta_{\text{SN}}$ . As in Parry et al. (2012) and Okamoto (2013), we suppose that only Type II SNe are responsible for driving winds and the energy released from Type Ia SNe is distributed as thermal energy to surrounding gas particles.

During any given time-step, a gas particle may receive supernova energy,  $\Delta Q$ , from one or more neighboring star particles. If this happens, the particle is given a probability,  $\mathcal{P}_w^{\text{SN}}$ , with which it becomes a wind particle during that time-step:

$$\mathcal{P}_w^{\text{SN}} = \frac{\Delta Q}{\frac{1}{2} m_{\text{SPH}} v_{w,\text{SN}}^2}, \quad (3)$$

where  $v_{w,\text{SN}}$  is the initial wind speed. The value of  $v_{w,\text{SN}}$  is defined to be proportional to the one-dimensional velocity dispersion of the neighboring dark matter particles,  $\sigma$ , namely,

$$v_{w,\text{SN}} = \kappa_w^{\text{SN}} \sigma, \quad (4)$$

where  $\kappa_w^{\text{SN}}$  is a proportional constant that defines the wind speed with respect to the local velocity dispersion. This scaling is motivated by the data on galactic outflows (Martin 2005). Okamoto et al. (2010) have shown that doing this reproduces the observed luminosity function and the luminosity-metallicity relation of the Local Group satellite galaxies. Puchwein & Springel (2013) have reported a good match to the faint end slope of the observed galaxy stellar mass function with this scaling.

### 2.2.2. Pre-supernova feedback

Stinson et al. (2013) identified that the lag between a star formation event and an SN explosion ( $\sim 10$  Myr) is likely to be a source of the difficulty for simulations in reproducing the observationally suggested relation between stellar mass and halo mass. They reproduced the relation by distributing 10 % of the bolometric luminosity emitted by young stars to the surrounding star-forming gas as thermal energy over 0.8 Myr time period before an SN goes off.

Recently some numerical studies have indicated the importance of radiation pressure feedback from young stars on galaxy evolution (Hopkins et al. 2011; Hopkins et al. 2012b; Chattopadhyay et al. 2012; Wise et al. 2012).

<sup>1</sup> We convert stellar mass and SFR obtained by assuming the Salpeter IMF (Salpeter 1955) and the Kroupa IMF (Kroupa 2001) into those with the Chabrier IMF by dividing them by 1.8 and 1.1, respectively.

Momentum injection by stellar winds also cannot be ignored (Hopkins et al. 2012b). Massive stars can radiatively drive stellar winds from their envelopes during the first stage of evolution, reaching terminal velocities of 1000–3000 km s<sup>−1</sup>. The momentum injection by the stellar winds is roughly the same order as that by the radiation pressure (Agertz et al. 2013). We thus consider the momentum driven winds (Oppenheimer & Davé 2006; Oppenheimer & Davé 2008) as the pre-SN feedback in this paper.

The momentum injection rate from radiation can be written as

$$\dot{p}_{\text{rad}} = (\eta_1 + \eta_2 \tau_{\text{IR}}) \frac{L(t)}{c}, \quad (5)$$

where  $\eta_1$  and  $\eta_2$  respectively define the momentum transfer efficiencies for the direct absorption/scattering and for the multi-scattering by infrared photons re-radiated by dust particles;  $\tau_{\text{IR}}$  is the infrared optical depth,  $L(t)$  is the luminosity of the stellar population, which we calculate using a population synthesis code PÉGASE (Fioc & Rocca-Volmerange 1997) as a function of the age and the metallicity of the star particle, and  $c$  is the speed of light.

The first term of equation (5) should be proportional to  $1 - \exp(-\tau_{\text{UV}})$ , where  $\tau_{\text{UV}}$  is the ultraviolet (UV) optical depth. Since the dust and H I opacities in the UV present in star-forming regions are very large, it is reasonable to assume that the value of  $\eta_1$  is around unity. The estimation of  $\tau_{\text{IR}}$  is problematic because we cannot resolve star-forming clouds in large volume simulations. We here simply assume that  $\tau_{\text{IR}}$  scales linearly with the metallicity of a star particle<sup>2</sup> (see Aumer et al. 2013 and Agertz et al. 2013 for more elaborate estimations of  $\tau_{\text{IR}}$ ). Under this assumption, equation (5) reduces to

$$\dot{p}_{\text{rad}}(Z, t) = \left[ \eta_1 + \tau_0 \left( \frac{Z}{Z_{\odot}} \right) \right] \frac{L(t)}{c}, \quad (6)$$

where  $\tau_0$  is  $\eta_2 \tau_{\text{IR}}$  at the solar metallicity. In our fiducial model, we set  $\eta_1 = 2$  since we do not explicitly consider momentum injection by stellar winds, the amount of which is the same order as that by the radiation pressure. We set  $\tau_0 = 30$ , which is consistent with the value found by Hopkins et al. (2011) who reported average infrared optical depth of  $\langle \tau_{\text{IR}} \rangle \sim 10 - 30$  in their high resolution simulated Milky Way-like galaxy.

During a time-step,  $\Delta t$ , a young star particle distributes the momentum and energy from radiation to surrounding gas particles. A gas particle thus may receive momentum,  $\Delta p_{\text{rad}}$ , and energy,  $\Delta E_{\text{rad}}$ , during any given time-step. The gas particle is selected to become a wind particle during that time-step with a probability,

$$\mathcal{P}_{\text{w}}^{\text{rad}} = \frac{\Delta p_{\text{rad}}}{m_{\text{SPH}} v_{\text{w,rad}}}, \quad (7)$$

<sup>2</sup> We must use the IR optical depth of a cloud in which the stellar population (i.e. star particle) is embedded. The metallicity of the cloud should be comparable to that of the stellar population because the stellar population inherits the metallicity of the parent cloud.

where  $v_{\text{w,rad}}$  is the initial wind speed of the momentum-driven wind. As for the SN-driven wind, we assume that the wind speed is proportional to the local velocity dispersion as

$$v_{\text{w,rad}} = \kappa_{\text{w}}^{\text{rad}} \sigma. \quad (8)$$

Since the role of the pre-SN feedback is to delay the star formation until the SN feedback takes place (Stinson et al. 2013), we assume  $\kappa_{\text{w}}^{\text{rad}} < \kappa_{\text{w}}^{\text{SN}}$  so that the expelled gas by the pre-SN feedback can fall back later. Okamoto et al. (2010) found that the winds with the initial wind speed of  $3\sigma$  are inefficient and have little effect on the luminosity function at  $z = 0$ . We hence employ  $\kappa_{\text{w}}^{\text{rad}} = 3$ .

Energy conservation should impose the limit on the mass-loading of the momentum-driven wind. The probability,  $\mathcal{P}_{\text{w}}^{\text{rad}}$ , then becomes

$$\mathcal{P}_{\text{w}}^{\text{rad}} = \min \left[ \frac{\Delta p_{\text{rad}}}{m_{\text{SPH}} v_{\text{w,rad}}}, \frac{\Delta E_{\text{rad}}}{\frac{1}{2} m_{\text{SPH}} v_{\text{w,rad}}^2} \right]. \quad (9)$$

The probability with which a gas particle is added to a wind is given as the sum of the two probability,  $\mathcal{P}_{\text{w}} = \mathcal{P}_{\text{w}}^{\text{SN}} + \mathcal{P}_{\text{w}}^{\text{rad}}$ , since they are independent events. We generate a uniform random number between zero and one. When  $\mathcal{P}_{\text{w}}$  exceeds this number, the gas particle is added to a wind. We determine whether the wind is SN- or radiation pressure-driven by drawing a uniform random number between zero and one again. If  $\mathcal{P}_{\text{w}}^{\text{SN}} / (\mathcal{P}_{\text{w}}^{\text{SN}} + \mathcal{P}_{\text{w}}^{\text{rad}})$  is greater than this number, the gas particle is launched as an SN-driven wind with  $v_{\text{w,SN}}$ , otherwise it becomes a radiation pressure-driven wind with  $v_{\text{w,rad}}$ . When the value of  $\mathcal{P}_{\text{w}}$  exceeds unity, we distribute its excess energy and momentum to its neighboring gas particles as described in Okamoto et al. (2010).

### 2.3. Quenching of gas cooling in large halos

It is now widely accepted that the stellar feedback alone cannot explain bright- (massive-) end of the galaxy luminosity (mass) function and a feedback process that operates preferentially in large halos is needed. (e.g. Benson et al. 2003). High resolution X-ray observations of galaxy clusters have revealed large, radio-plasma cavities in intracluster media (ICM). These are usually associated with episodic outbursts from a central radio galaxy, and indicate that huge amounts of mechanical energy are being deposited into the ICM by powerful AGN-driven jets (Bîrzan et al. 2004; Allen et al. 2006; Fabian et al. 2006; Taylor et al. 2006). Simulations investigating the impact of these AGN-driven radio cavities suggest that this powerful feedback provides sufficient energy to offset the cooling radiation from the cluster and potentially explains why so little cool gas is seen in these systems (Quilis et al. 2001; Churazov et al. 2002; Dalla Vecchia et al. 2004; Omma et al. 2004; Sijacki & Springel 2006).

Simple prescriptions for the feedback from AGN jets (aka. ‘radio-mode feedback’) have been incorporated into semi-analytic galaxy formation models (e.g. Croton et al. 2006; Bower et al. 2006). Including radio-mode AGN feedback has resulted in dramatic improvements in the

models' ability to match the sharp decline of the galaxy luminosity function and to explain the 'downsizing' seen in the evolution of the galaxy population. Bower et al. (2006) showed that, by assuming that AGN radio-mode feedback operates only in quasi-hydrostatic halos where the cooling time is longer than the dynamical time, the galaxy luminosity functions in local and higher redshift universe can be matched well.

In order to model the AGN radio-mode feedback, Sijacki et al. (2007) and Okamoto et al. (2008b) distinguished two fundamentally different modes of AGN accretion: radiatively efficient, geometrically thin accretion flows (standard disks: Shakura & Sunyaev 1973) and geometrically thick, radiatively inefficient accretion flows (which we will generically refer to as RIAFs; Narayan et al. 1998; Narayan 2005). They assumed only the latter is responsible for the radio-mode feedback through production of powerful jets (e.g. Rees et al. 1982; Meier 2001; Maccarone et al. 2003; Churazov et al. 2005). Since RIAFs exist only when the accretion rate is much lower than the Eddington rate (Narayan et al. 1998), the radio-mode feedback is naturally switched on in cooling inefficient large halos where central blackholes become very massive and gas supply to them is slowed down (Sijacki et al. 2007; Okamoto et al. 2008b).

We however take a simpler, phenomenological approach in this paper because modeling AGN feedback inevitably introduces many uncertainties, such as seed blackhole mass, accretion rates onto blackholes, blackhole mergers, and feedback from AGN. In our phenomenological treatment, we simply assume that the radiative cooling is suppressed in large halos where one-dimensional dark matter velocity dispersion is larger than  $\sigma_{\text{th}}(z)$ . We parameterize the functional form of  $\sigma_{\text{th}}(z)$  as

$$\sigma_{\text{th}}(z) = \sigma_0(1+z)^\alpha, \quad (10)$$

where the parameter,  $\alpha$ , controls the redshift dependence. In order to reduce cooling in large halos, we modify the cooling function,  $\Lambda(T, Z)$  as

$$\Lambda(T, Z, \sigma) = \begin{cases} \Lambda(T, Z) & (\sigma < \sigma_{\text{th}}) \\ \Lambda(T, Z) \exp\left(-\frac{\sigma - \sigma_{\text{th}}}{\beta \sigma_{\text{th}}}\right) & (\text{otherwise}) \end{cases}, \quad (11)$$

where the parameter,  $\beta$ , specifies how steeply the cooling is suppressed above the threshold velocity dispersion,  $\sigma_{\text{th}}$ . We find that a sudden suppression, i.e.  $\Lambda(T, Z, \sigma) = 0$  for  $\sigma > \sigma_{\text{th}}$  creates an unwanted bump around the mass corresponding to  $\sigma_{\text{th}}$  in the galaxy stellar mass function. To mimic the AGN radio-mode feedback,  $\alpha$  must be greater than 0 since the velocity dispersion of a cooling inefficient halo increases with increasing redshift and, for given velocity dispersion of a halo, the central blackhole mass is likely to become smaller with increasing redshift<sup>3</sup>. We adopt  $\alpha = 0.75$  and  $\beta = 0.3$  in our fiducial model (Croton et al. 2006; Nagashima et al. 2005). As we will show later,

<sup>3</sup> Without the redshift dependence (i.e.  $\alpha = 0$ ), it is still possible to obtain a galaxy stellar mass function compatible with observational estimates at  $z = 0$ . We however lack massive galaxies at higher redshift in this case (see Shimizu et al. 2012).

this choice makes the quenching almost negligible at high redshift ( $z > 2$ ) because  $\sigma_{\text{th}}$  becomes large and halos that have higher velocity dispersion than  $\sigma_{\text{th}}$  are quite rare. We note that the comparable results to this set of parameters can be obtained with  $\sigma_0 \simeq 100 \text{ km s}^{-1}$  if we assume a sudden suppression of the gas cooling above  $\sigma_{\text{th}}$ .

## 2.4. Models

We list the values of the model parameters in Table 1, which we choose to match the observational estimates of the stellar mass functions and the stellar mass fractions from  $z = 4$  to 0. We show several combinations of the above feedback processes in order to highlight roles of each process. We refer to the SN feedback, the radiation pressure feedback, and the quenching of the cooling in large halos as 'SN', 'RP', and 'AGN', respectively, for short. In this paper, we show the models; 'SN', 'SN+RP', 'SN+AGN', and 'SN+RP+AGN'. The model that employs all the feedback processes, 'SN+RP+AGN', is our fiducial model. The model that only considers the SN feedback, 'SN', corresponds to the model we used in our previous studies (Shimizu et al. 2011; Shimizu et al. 2012; Shimizu et al. 2013), although the values of the parameters in these studies are slightly different from those in this paper mainly due to the differences in the numerical resolution and cosmology.

## 3. Results

In this section, we compare our simulations with the available observational estimates from  $z = 4$  to 0 and show effects of each feedback process. To identify virialized dark matter halos, we first run the friends-of-friends (FoF) group finder (Davis et al. 1985) with a linking length 0.2 in units of the mean dark matter particle separation. Gas and star particles near dark matter particles which compose a FoF group are also regarded as the member of the group. We then identify gravitationally bound groups of dark matter, gas, and stars in each FoF group by using the SUBFIND algorithm (Springel et al. 2001). We regard a gravitationally bound group of particles that consists of at least 32 particles and contains at least 10 star particles as a 'galaxy'. We do not discriminate between satellite and central galaxies in our analyses unless otherwise stated. In order to exclude diffusely distributed stellar component (Zibetti et al. 2005; McGee & Balogh 2010) from the stellar component of a galaxy, we define the galactic stellar mass as the sum of stellar mass within twice the stellar half mass radius as done in Vogelsberger et al. (2013).

### 3.1. Stellar mass

Since we have chosen the model parameters so that to reproduce the observationally estimated stellar mass functions and stellar mass fractions as functions of the halo mass, we first show how the simulations compare to these estimates. In figure 1, we show the simulated galaxy stellar mass functions at  $z = 4, 3, 2, 1, 0.5$ , and 0. We also plot the observational estimates at each redshift.

We note that all the models agree with the observa-

**Table 1.** Model parameters

$c_*$	$\eta_{\text{SN}}$	$\kappa_{\text{w}}^{\text{SN}}$	$\kappa_{\text{w}}^{\text{rad}}$	$\eta_1$	$\tau_0$	$\sigma_0$	$\alpha$	$\beta$
0.01	0.4	3.5	3.0	2.0	30	(km s <sup>-1</sup> ) 50	0.75	0.3

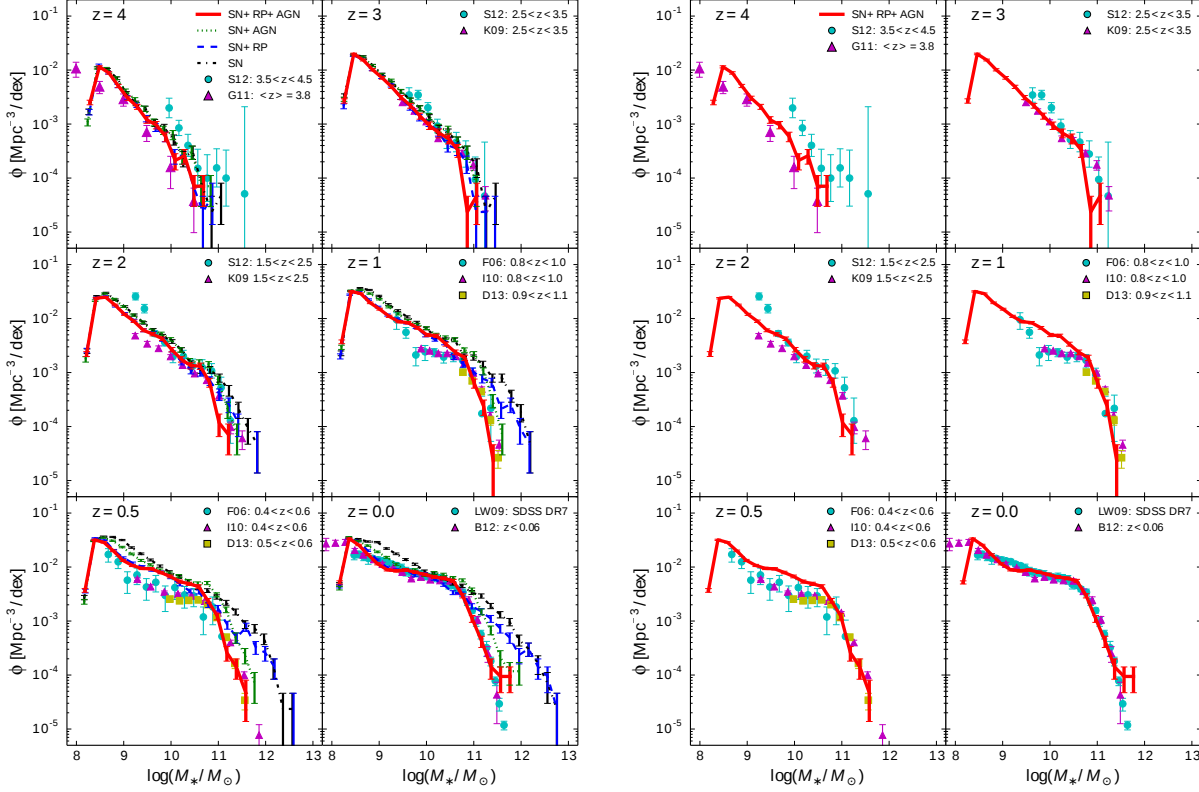


**Fig. 1.** Simulated galaxy stellar mass functions. *Left:* The red solid, green dotted, blue dashed, and black dot-dashed lines illustrate the results from ‘SN+RP+AGN’, ‘SN+AGN’, ‘SN+RP’, and ‘SN’, respectively. The error bars represent the  $1\sigma$  Poisson error. The observational estimates at six different redshifts are also plotted as the symbols with error bars. The data sources are Santini et al. (2012) (S12) and González et al. (2011) (G11) for  $z = 4$ , S12 and Kajisawa et al. (2009) (K09) for  $z = 3$  and 2, Fontana et al. (2006) (F06), Ilbert et al. (2010) (I10), and Davidzon et al. (2013) (D13) for  $z = 1$  and 0.5, and Li & White (2009) (LW09) and Baldry et al. (2012) (B12) for  $z = 0$ . *Right:* Same as in the left panels, but we only show the fiducial model, ‘SN+RP+AGN’, for easier comparison with the observational estimates.

tional estimates at  $z \geq 2$ . This fact may validate our previous studies of the high redshift galaxy populations (Shimizu et al. 2011; Shimizu et al. 2012; Shimizu et al. 2013) where we only considered the SN-driven winds. At  $z < 2$ , however, the models without ‘AGN’ form far too many massive galaxies, confirming that some quenching mechanism of the gas cooling in large halos is needed. Both ‘SN+AGN’ and ‘SN+RP+AGN’ reproduce the observed galaxy stellar mass functions at all six redshifts reasonably well. For easier comparison with the observational estimates, we show the fiducial model, ‘SN+RP+AGN’ in the right panels of figure 1.

The role of the radiation pressure-driven winds, ‘RP’, are not evident from this analysis. We shall investigate it in more detail by looking at the galaxy formation efficiency as function of the halo mass.

The technique called abundance matching places galax-

ies in the same stellar mass ranking as the dark matter halo mass rank (Conroy & Wechsler 2009; Behroozi et al. 2010; Guo et al. 2010; Moster et al. 2013; Behroozi et al. 2013). Using this technique, a detailed link between observed galaxy stellar mass and their host halo mass has been obtained and it puts a strong constraint on galaxy formation models (see Moster et al. 2013).

In figure 2, we compare the simulated stellar mass fraction,  $M_*/M_{200}$ , for the central galaxies with that obtained by the abundance matching technique taken from Moster et al. (2013), where  $M_{200}$  is defined as the sum of all mass within a sphere whose average density is 200 times the critical density. We only show halos that contains more than 100 dark matter particles since the analysis is limited to the central galaxy whose dark halos do not suffer from the tidal stripping. It is evident that the models without ‘AGN’ convert too many baryons into the stars

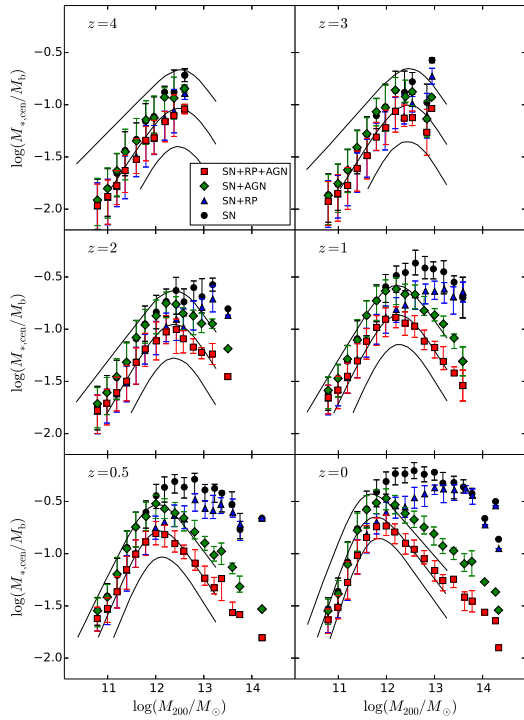


**Fig. 2.** Central galaxy formation efficiencies at  $z = 4, 3, 2, 1, 0.5$ , and  $0$  as functions of the halo mass. We show the median stellar mass fraction for the simulated galaxies; The red squares, green diamonds, blue triangles, and black circles indicate ‘SN+RP+AGN’, ‘SN+AGN’, ‘SN+RP’, and ‘SN’, respectively. An error bar indicates the 25th to the 75th percentile of the distribution in each halo mass bin. The thick black solid lines indicates the average galaxy formation efficiencies estimated by (Moster et al. 2013) using an abundance matching model; the thin black lines show the  $1\sigma$  confidence level.

in the massive halos and cannot reproduce the characteristic mountain-shaped curve inferred from the abundance matching model. On the other hand, the models without ‘RP’ predict slightly higher stellar fractions in low mass halos ( $M_{200} \lesssim 10^{12} M_{\odot}$ ) at redshift between 1 and 0.5; the pre-SN feedback brings a better match to the result obtained by the abundance matching model as suggested by the earlier studies (Aumer et al. 2013; Kannan et al. 2013).

We note that ‘RP’ lowers the galaxy formation efficiencies in massive halos more strongly than in low mass halos. There are two reasons why the radiation pressure feedback operates in large halos. Firstly, the mass-loading of the momentum-driven winds is proportional to  $\sigma^{-1}$  which is larger than that of the energy-driven winds ( $\propto \sigma^{-2}$ ) in large halos. Secondly, the metallicity is higher in larger halos as we will show later and hence more momentum per star formation is injected in larger halos. By combining all these effects, our fiducial model reproduces the result by the abundance matching model quite well at all redshifts from  $z = 4$  to  $0$ .

We have shown that there exists a combination of the parameters that can reproduce the evolution of galaxy stellar mass from  $z = 4$  to  $0$ . In the following subsections,

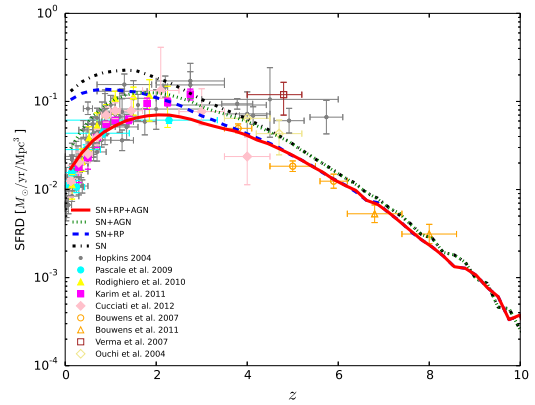


**Fig. 3.** Evolution of the cosmic star formation rate densities. The red solid, green dotted, blue dashed, and black dot-dashed lines illustrate the results from ‘SN+RP+AGN’, ‘SN+AGN’, ‘SN+RP’, and ‘SN’, respectively. We also show observational constraints; the data are taken from Hopkins (2004; gray dots), Pascale et al. (2009; cyan filled circles), Rodighiero et al. (2010; yellow filled triangles), Karim et al. (2011; magenta filled squares), Cucciati et al. (2012; pink filled diamonds), Bouwens et al. (2007; orange open circles), Bouwens et al. (2011; orange open triangles), Verma et al. (2007; brown open squares), and Ouchi et al. (2004; khaki open diamonds).

we shall examine other observables, such as star formation rate and metallicity, and the roles of each feedback process. We use only the galaxy stellar mass functions and the galaxy formation efficiencies to set our model parameters. The properties of the galaxies in the following subsections are simply *outcomes* of our simulations.

### 3.2. Star formation rate

The star formation rate (SFR) tells us how the stellar component in the galaxies is build up and how many ionizing photons are produced. In figure 3, we show the simulated cosmic star formation rate densities as functions of redshift. The models that only have the stellar feedback, i.e. ‘SN’ and ‘SN+RP’, fail to reproduce the steep decline of the SFR density toward lower redshift at  $z < 2$ . This suggests that the quenching of the gas cooling in large halos is responsible for this decline. By comparing the models with and without the radiation pressure feedback, we find that the effect of this feedback is most pronounced at the redshift where the SFR density is maximum ( $z \simeq 2$ ). This effect makes ‘SN+RP+AGN’ more successful in matching the galaxy formation efficiency to that inferred from the abundance matching technique at  $z < 2$  (figure 2). As for the cosmic SFR density, both ‘SN+AGN’ and ‘SN+RP+AGN’ agree with the observational constraints reasonably well.

Observationally, normal star-forming galaxies lie on the so-called the main sequence of the star-forming galaxies, which describes the relation between galactic stellar mass and star formation rate (e.g. Brinchmann et al. 2004; Noeske et al. 2007; Daddi et al. 2007). The normalization of the relationship evolves with redshift while its slope remains nearly constant. The small scatter of the rela-



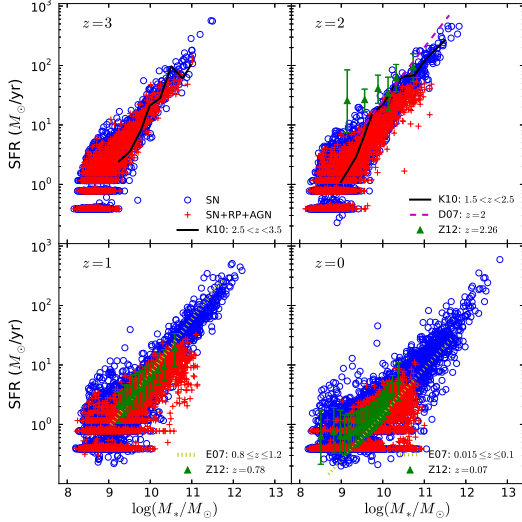


**Fig. 4.** Star formation rates against stellar masses. Since the difference between the models are quite small, we only show the results by ‘SN’ (blue open circles) and ‘SN+RP+AGN’ (red plus signs). The observational estimates by Kajisawa et al. (2010; K10), Daddi et al. (2007; D07), Elbaz et al. (2007; E07), and Zahid et al. (2012; Z12) are respectively indicated by the black solid lines, the magenta dashed line, the yellow dotted lines, and the green filled triangles.

tionship implies that most of the stellar mass of galaxies have been developed along this sequence (Noeske et al. 2007).

In figure 4, we compare the simulated SFRs as functions of the galactic stellar mass with the several observational estimates at  $z = 3, 2, 1$ , and  $0$ . For the simulations, we estimate the SFR in a galaxy from the mass of stars that were born in the past 100 Myr. Note that we plot all the galaxies that have non-zero SFRs. Since the difference between the models is quite small except for massive galaxies, we only show the most distinctive two models, ‘SN’ and ‘SN+RP+AGN’.

We find that our simulations agree with the observational estimates well. The slopes of the median SFRs as functions of the stellar mass (not shown) are  $\simeq 0.9$  for  $z = 3, 2$ , and  $1$ , and  $\simeq 0.8$  for  $z = 0$  also agree with the observational estimates (e.g. Elbaz et al. 2007). While the simulated SFRs fall slightly below the observational estimates at  $z = 2$ , boosting the SFRs at this redshift would result in enhancing the offset between the simulated and the observationally suggested galaxy stellar mass functions at  $z = 1$  and  $0.5$  (see figure 1).

The effect of the quenching of the gas cooling is seen even at  $z = 3$ . The absence of galaxies with very high SFRs ( $\gg 100 M_{\odot} \text{ yr}^{-1}$ ), which exist in the SN-only simulation, may affect our predictions about sub-mm galaxies (Shimizu et al. 2012). We defer the investigation of this issue to future studies.

Observationally, the galaxy stellar mass at which the SFR starts to drop strongly decreases with time (e.g. Cowie et al. 1996). To examine when the stellar mass of the simulated galaxies is built up, we show the luminosity

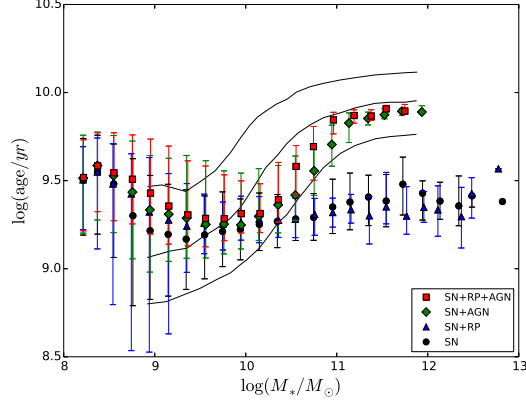


**Fig. 5.** Luminosity-weighted stellar ages as functions of the stellar mass at  $z = 0$ . We show the median  $V$ -band weighted stellar age for the simulated galaxies. The red squares, green diamonds, blue triangles, and black circles indicate ‘SN+RP+AGN’, ‘SN+AGN’, and ‘SN’, respectively. An error bar indicates the 16th to the 84th percentile of the distribution in each stellar mass bin. The increase of the stellar age toward the lower stellar mass from  $M_{*} \simeq 10^{9.5} M_{\odot}$  is a numerical effect (see section 4). The thick solid line indicates the observational estimate by Gallazzi et al. (2005) and thin solid lines represent the 16th to the 84th percentile of the distribution.

weighted stellar ages as functions of the stellar mass at  $z = 0$  in figure 5. We also show the observational estimate by Gallazzi et al. (2005) for comparison.

Without the quenching of the gas cooling in large halos, the stellar age is nearly constant as a function of the stellar mass. The introduction of the quenching makes the stellar age older for  $M_{*} \gtrsim 10^{10} M_{\odot}$  and both ‘SN+AGN’ and ‘SN+RP+AGN’ broadly agree with the observational estimate. The inclusion of the radiation pressure feedback does not make a big difference, that is, ‘SN’ and ‘SN+RP’ are very similar to each other. By combined with the quenching, however, the radiation pressure feedback makes the stellar age older at  $10^{10-11} M_{\odot}$  and ‘SN+RP+AGN’ better agrees with the observation than ‘SN+RP’. All the models show the increase of the stellar age toward the lower stellar mass from  $M_{*} \sim 10^{9.5} M_{\odot}$ . This increase is caused by our stochastic treatment of the star formation and insufficient numerical resolution (see the resolution study in section 4). Our results suggest that the quenching of the cooling in large halos is essential to explain the galaxy downsizing.

### 3.3. Metallicity

We now investigate the metallicity of galaxies which is a sensitive diagnostic of the feedback physics. In particular, the mass-metallicity relation is very sensitive to the winds properties (Oppenheimer & Davé 2008; Okamoto et al. 2010).

Observationally, the nebula metallicity of galaxies is determined by measuring a ratio (or ratios) of emission lines that are usually emitted from H II and photo-dissociation regions. These lines come from the star forming regions. In order to compare our results with such observations,



we employ the nebula metallicity introduced by Shimizu et al. (2013), which is defined as the Lyman continuum weighted metallicity. In this definition, only the metals around the very young star particles are taken into account.

In figure 6, we show the mass-metallicity relations at  $z = 3, 2, 1.5, 0.75$ , and 0 and compare them with the several observational estimates. There are uncertainties in defining the metallicity from a ratio (or ratios) of emission lines (Nagao et al. 2006; Kewley & Ellison 2008). We have thus converted all the data into the Pettini & Pagel (2004, hereafter PP04) diagnostic. For the conversion between the PP04 and Kobulnicky & Kewley (2004) diagnostics, we apply an empirical conversion of Kewley & Ellison (2008). We use the relation by Nagao et al. (2006) to convert the metallicity of Mannucci et al. (2009) into that by the PP04 diagnostic. Note that because of the uncertainties in the observed metallicity and theoretical nucleosynthesis yields (Wiersma et al. 2009b), the normalization of the mass-metallicity relation is less important than its slope and relative redshift evolution of the relationship.

We find that all the models show similar slopes at high redshift ( $z \geq 2$ ). At low redshift, however, the models without the radiation pressure feedback have slightly steeper profiles than those with the radiation pressure feedback. These models also show stronger redshift evolution than the models with the radiation pressure. This is because the radiation pressure feedback becomes stronger in higher metallicity star-forming regions (equation (6)) and therefore it slows down the metal enrichment efficiently. Consequently, the models without the radiation pressure feedback show slightly too strong redshift evolution compared with the observations. Our fiducial model, ‘SN+RP+AGN’, produces the mass-metallicity relation that is broadly consistent with the observational estimates, including the slope and the redshift evolution of the normalization because of the strong outward winds (see the left panels). We note that we would obtain slightly higher metallicity if we had included metal diffusion because the diffusion leads to outflowing particles losing metals to the circum-galactic medium (Shen et al. 2010; Aumer et al. 2013). The strange bump seen in the mass-metallicity relations at  $M_* \simeq 10^9 M_\odot$  is due to the quantized star formation and insufficient resolution. The resolution study we will present in the next section shows that the bump moves to lower mass when we increase the resolution.

#### 4. Resolution dependence

It is important to know how simulation results depend on an adopted numerical resolution and what parameters we should adjust when we change the resolution. For this purpose, we perform two additional simulations with the same parameter set as ‘SN+RP+AGN’, to which we refer as ‘L40N256E40’ in this section, but with higher and lower numerical resolutions. The simulations that employ 8 times higher and 8 times lower mass resolutions are called

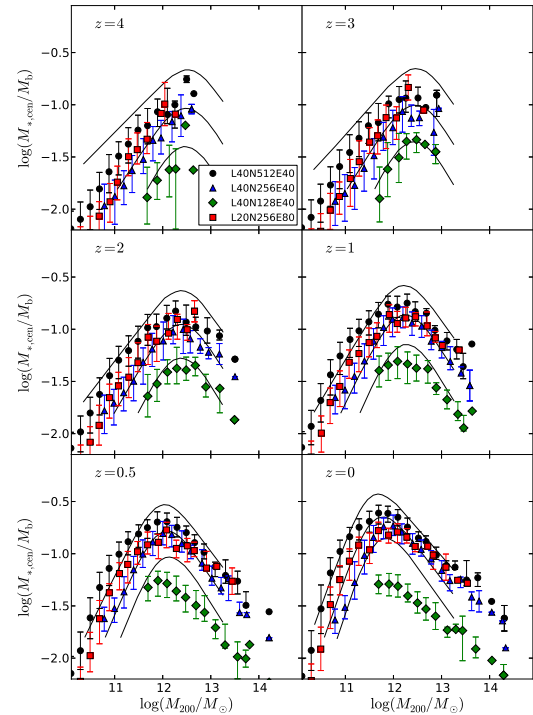


**Fig. 7.** Central galaxy formation efficiencies in different resolution simulations. The black circles, blue triangles, and green diamonds represent the results from L40N512E40, L40N256E40, and L40N128E40, respectively. We also show the simulation with the same resolution with L40N512E40 but with different feedback parameters and a smaller simulation volume, which is indicated by the red squares (L20N256E80).

‘L40N512E40’ and ‘L40N128E40’, respectively. A gravitational softening length is a factor of 2 shorter (longer) in L40N512E40 (L40N128E40) than that in L40N256E40. We also change the star formation threshold density,  $n_{\text{th}}$ , as a function of the numerical resolution; we adopt a density that is higher by a factor of 4 for a mass resolution that is higher by a factor of 8 as done in Okamoto (2013) to improve the numerical convergence (see also Parry et al. 2012).

In figure 7, we compare the central galaxy formation efficiencies obtained from the three different resolution simulations. We find that our results are converging, i.e. the result from the intermediate resolution simulation is much closer to that from the high resolution one than that from the low resolution one. We also find that the simulations have not converged at the current resolution yet, i.e. the results from the high and intermediate resolution simulations do not agree with each other. In general, star formation in smaller halos is resolved with higher resolution and hence more stars form in a higher resolution simulation until a simulation resolves the smallest halo that can form stars after reionization ( $\sim 10^8 M_\odot$ ; see Okamoto et al. 2008a and Okamoto et al. 2010). When a halo is more poorly resolved, winds may more easily escape from the halo to the intergalactic space. These two factors explain the resolution dependence seen in figure 7.

Since the offset is observed mainly for the low mass

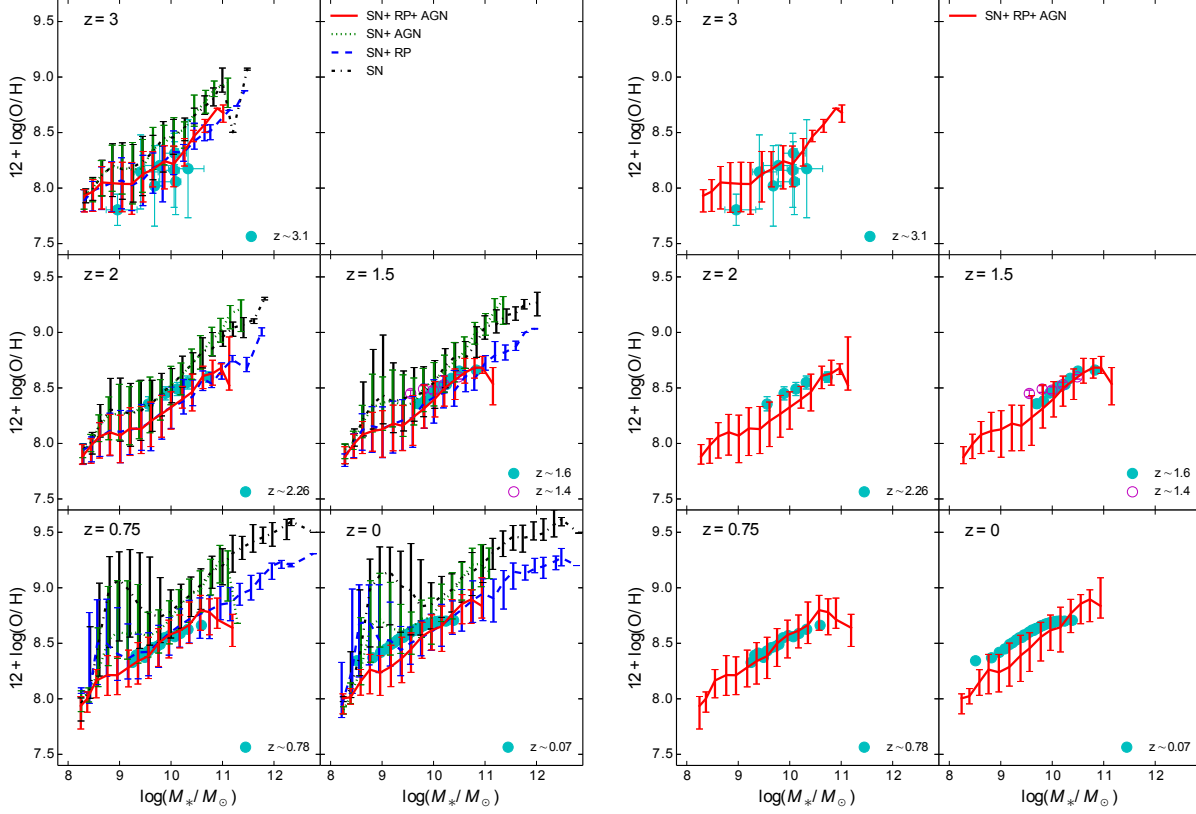


**Fig. 6.** The nebula metallicities of the simulated galaxies as functions of the stellar mass at  $z = 3, 2, 1.5, 0.75$ , and  $0$ . *Left:* The binned medians for ‘SN+RP+AGN’, ‘SN+AGN’, ‘SN+AGN’, and ‘SN’ are indicated by the red solid, green dotted, blue dashed, and black dash-dotted lines, respectively. An error bar indicates the 25th to the 75th percentile of the distribution in each mass bin. Observational estimates around the presented redshifts are also shown. The filled symbols in the panel for  $z = 3$  are those by Mannucci et al. (2009). The filled symbols in the panels for  $z = 2, 0.75$ , and  $0$ , are the observational estimates compiled by Zahid et al. (2012). For  $z = 1.5$ , estimates by Zahid et al. (2013) and Yabe et al. (2014) are indicated by the filled and open symbols, respectively. *Right:* Same as in the left panels, but we only show the fiducial model, ‘SN+RP+AGN’, for easier comparison with the observational estimates.

halos, we may obtain a comparable result to the fiducial simulation (L40N256E40) by enhancing the stellar feedback in the high resolution simulation. To test this, we also show the result from the simulation whose resolution is the same as L40N256E40 but with different values of the feedback parameters. In this simulation we increase the SN feedback efficiency from  $\eta_{\text{SN}} = 0.4$  to  $0.8$  and the value of  $\tau_0$  in the radiation pressure feedback from  $30$  to  $40$ . Other parameters are remain fixed to the fiducial values. In order to save the computational time, we use a smaller simulation box size,  $20 h^{-1}$  Mpc, for this simulation. We call this additional simulation ‘L20N256E80’. The result from this simulation is also shown in figure 7, which is comparable to the fiducial simulation and consistent with the estimate by the abundance matching technique. We have confirmed that the same conclusion can be drawn from the galaxy stellar mass function.

Next we show resolution effects on the stellar age. In figure 8, we compare the stellar ages as functions of the stellar mass in the three different resolution simulations. The low resolution simulation exhibits rather old stellar age for all the mass range. The results from the high and intermediate resolution simulations agree with each other

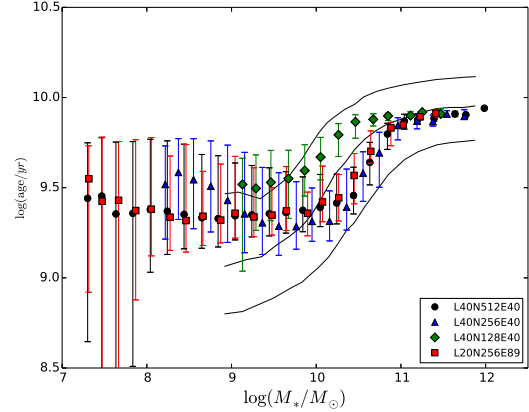


**Fig. 8.** Luminosity-weighted stellar ages in different resolution simulations. The black circles, blue triangles, and green diamonds represent the results from L40N512E40, L40N256E40, and L40N128E40, respectively. We also show the simulation with the same resolution with L40N512E40 but with different feedback parameters and a smaller simulation volume, which is indicated by the red squares (L20N256E80).

well, indicating the results almost converge for the stellar age at the intermediate resolution. By comparing the three simulations, we conclude the upturn in the stellar age toward lower stellar mass is purely a numerical effect since it occurs at much lower mass in the high resolution simulation.

We also show the high resolution simulation with stronger feedback (L20N256E80). Interestingly, the result is almost identical to that from the high resolution simulation (L40N512E40) in spite of the difference in the galaxy formation efficiency (see figure 7). We note that the stellar age is nearly constant below  $10^{10} M_{\odot}$  in both of the two high resolution simulations, where the observationally estimated stellar age gradually decreases toward lower mass. This discrepancy seems to indicate that our galaxy formation model is still too simple and that processes which make the star formation time-scale longer in smaller galaxy are required, although the simulation results are still broadly consistent with the observational estimate at  $10^9 \lesssim M_* \lesssim 10^{10} M_{\odot}$ .

Finally we investigate resolution effects on the mass-metallicity relation. In figure 9, we show the nebula metallicities as functions of the stellar mass in the three different resolution simulations. We find that the slopes well converge and that all the simulations show similar redshift evolution. We also find that the bump seen at low-mass end is purely a resolution effect. The bump moves to lower mass when we increase the resolution. A higher resolution simulation exhibits higher metallicity indicating that the feedback effect is weaker in a higher resolution simulation. The high resolution simulation with stronger feedback (L20N256E80) recovers the result from the fiducial simulation (L40N256E40). The result from L20N256E80 is highlighted in the right panels, which shows that it is, in fact, very similar to that from L40N256E40 shown in the right panels of figure 6.

## 5. Summary and discussion

We have updated the galaxy formation model described by Okamoto et al. (2010) to study evolution of galaxy population. The new model employs suppression of gas cooling in large halos and momentum injection by radiation pressure from massive stars in addition to SN feedback. We normalize the model parameters so that the fiducial simulation matches the observationally estimated stellar mass functions and galaxy formation efficiencies from  $z = 4$  to 0. Interestingly, the fiducial model also well reproduces other observational properties of galaxy population: the cosmic star formation rate density, the main sequence of star-forming galaxies, the stellar age-stellar mass relation, and the mass-metallicity relation over a wide range of redshift.

In order to investigate the roles of individual feedback processes, we have performed the simulations by switching on and off each of them alternately. The suppression of the gas cooling in large halo, which we view as a phenomenological treatment of the radio mode AGN feedback, is necessarily to explain the high mass-end of the galaxy stellar

mass functions and the decline of the cosmic star formation rate density at low redshift. Our simple quenching model well describes the star formation properties in massive galaxies. This process makes the stellar age of massive galaxies older and nicely reproduces the galaxy downsizing for massive galaxies with  $M_* \gtrsim 10^{10} M_{\odot}$ . On the other hand, our high resolution simulations show that the stellar age of the less massive galaxies is nearly constant for  $M_* \lesssim 10^{10} M_{\odot}$ , while the observations suggest that the less massive galaxies have younger stellar age. This discrepancy for the low mass galaxies might suggest that our galaxy formation model is still too simple and we need processes that make effective star formation time-scale longer in smaller galaxies.

When we do not consider the radiation pressure feedback, the redshift evolution of the mass-metallicity relation is slightly too strong and the slope of the relation is too steep at low redshift. The metallicity dependence of the radiation pressure feedback helps to make the simulation result broadly consistent with the observational estimates. This fact provides a strong case for the radiation pressure feedback.

We find that the introduction of the AGN-like feedback and the radiation pressure feedback little affects the results at high redshift ( $z > 2$ ). We thus expect that our conclusions derived from the simulations of high redshift galaxy population (Shimizu et al. 2011; Shimizu et al. 2012; Shimizu et al. 2013; Inoue et al. 2014), which only take the SN feedback into account, still hold. However the lack of the galaxies with  $\text{SFR} \gg 100 M_{\odot} \text{ yr}^{-1}$  at  $z > 2$ , which exist in ‘SN’ model, might become a problem to account for the sub-mm source number counts. We leave this issue for future work.

The resolution study shows that the simulation results are converging numerically although the perfect numerical convergence has not been achieved at the current resolution. We show that, from a high resolution simulation, consistent results with the intermediate resolution simulation can be obtained by applying slightly stronger stellar feedback while the AGN-like feedback is remain unchanged. We expect that we would need little change in the parameter values if we employed even higher resolution because the simulation results in Okamoto et al. (2010) and Okamoto (2013) nicely converged with  $m_{\text{SPH}}^{\text{orig}} \lesssim 10^7 M_{\odot}$  for Milky Way-sized galaxies and with  $m_{\text{SPH}}^{\text{orig}} \lesssim 10^6 M_{\odot}$  even for the Local Group satellite galaxies.

The new model can apply for wider ranges of redshift and mass than the previous model that forms too massive galaxies in large halos, in particular, at low redshift. This simple model is well suited for simulations that relate high redshift galaxy population to the local one and for studies of coevolution of cluster galaxies and an ICM.

We would like to thank Ryu Makiya and Masahiro Nagashima for helpful discussion. Numerical simulations were carried out with Cray XC30 in CfCA at NAOJ and T2K-Tsukuba in Center for Computational Sciences at University of Tsukuba. TO acknowledges the financial support of Japan Society for the Promotion of Science

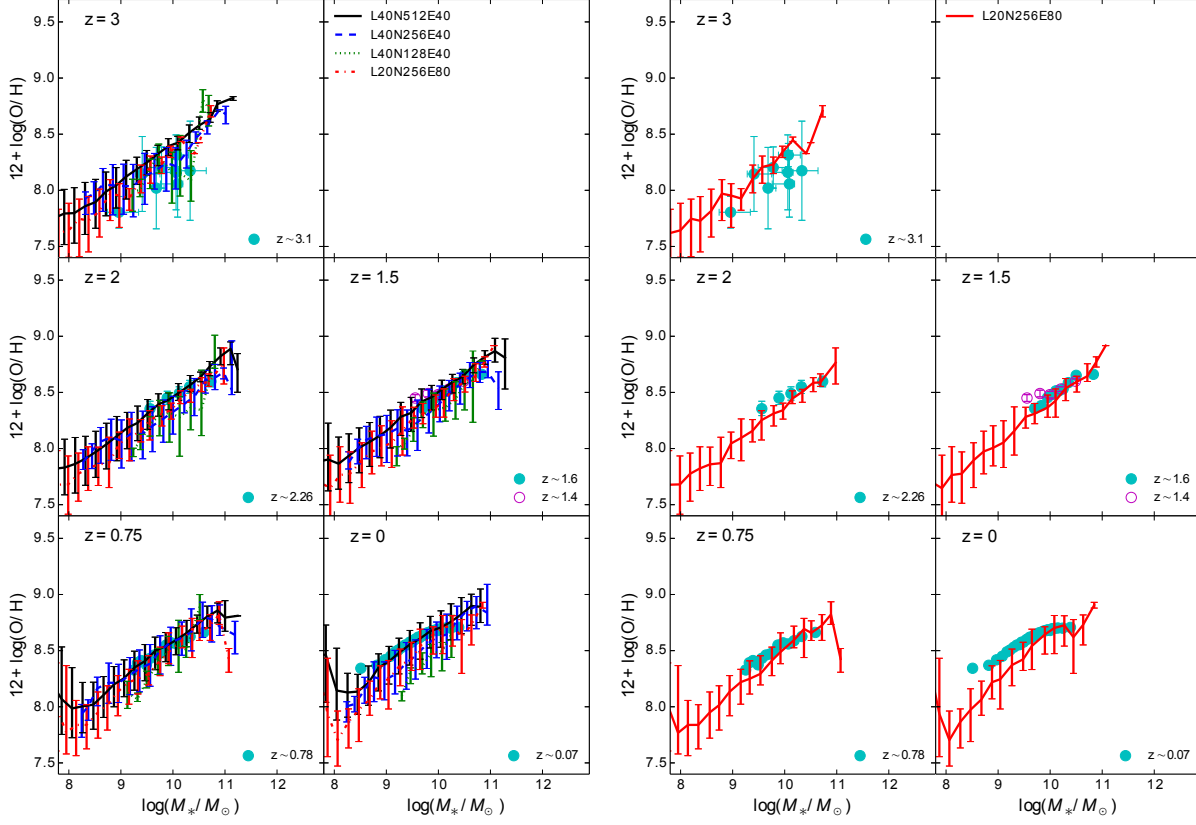


**Fig. 9.** The nebula metallicity of the galaxies in different resolution simulations. *Left:* The black solid, blue dashed, green dotted lines represent the results from L40N512E40, L40N256E80, and L40N128E40, respectively. The red-dotted lines indicate the simulation with the same resolution as L40N512E40 but with different feedback parameters and a smaller box size (L20N256E80). *Right:* Same as in the left panels but we only show L20N256E80 by the red solid lines for easier comparison with the observational estimates.

(JSPS) Grant-in-Aid for Young Scientists (B: 24740112). IS acknowledges the financial support of JSPS Grant-in-Aid for Young Scientists (A: 23684010). YN acknowledges the financial support of JSPS Grant-in-Aid for Scientific Research (25287050) and the FIRST program Subaru Measurements of Images and Redshifts (SuMIRE) by the Council for Science and Technology Policy.

## References

- Agertz, O., Kravtsov, A. V., Leitner, S. N., & Gnedin, N. Y. 2013, *The Astrophysical Journal*, 770, 25
- Agertz, O., Moore, B., Stadel, J., et al. 2007, *MNRAS*, 380, 963
- Allen, S. W., Dunn, R. J. H., Fabian, A. C., Taylor, G. B., & Reynolds, C. S. 2006, *MNRAS*, 372, 21
- Aumer, M., White, S. D. M., Naab, T., & Scannapieco, C. 2013, *MNRAS*, 434, 3142
- Baldry, I. K., Driver, S. P., Loveday, J., et al. 2012, *MNRAS*, 421, 621
- Behroozi, P. S., Conroy, C., & Wechsler, R. H. 2010, *ApJ*, 717, 379
- Behroozi, P. S., Wechsler, R. H., & Conroy, C. 2013, *ApJ*, 770, 57
- Benson, A. J., Bower, R. G., Frenk, C. S., et al. 2003, *ApJ*, 599, 38
- Birzan, L., Rafferty, D. A., McNamara, B. R., Wise, M. W., & Nulsen, P. E. J. 2004, *ApJ*, 607, 800
- Bouwens, R. J., Illingworth, G. D., Franx, M., & Ford, H. 2007, *ApJ*, 670, 928
- Bouwens, R. J., Illingworth, G. D., Oesch, P. A., et al. 2011, *ApJ*, 737, 90
- Bower, R. G., Benson, A. J., Malbon, R., et al. 2006, *MNRAS*, 370, 645
- Boylan-Kolchin, M., Springel, V., White, S. D. M., Jenkins, A., & Lemson, G. 2009, *MNRAS*, 398, 1150
- Brinchmann, J., Charlot, S., White, S. D. M., et al. 2004, *MNRAS*, 351, 1151
- Chabrier, G. 2003, *PASP*, 115, 763
- Chattopadhyay, I., Sharma, M., Nath, B. B., & Ryu, D. 2012, *MNRAS*, 423, 2153
- Churazov, E., Sazonov, S., Sunyaev, R., et al. 2005, *MNRAS*, 363, L91
- Churazov, E., Sunyaev, R., Forman, W., & Böhringer, H. 2002, *MNRAS*, 332, 729
- Cole, S., Lacey, C. G., Baugh, C. M., & Frenk, C. S. 2000, *MNRAS*, 319, 168
- Conroy, C., & Wechsler, R. H. 2009, *ApJ*, 696, 620
- Cowie, L. L., Songaila, A., Hu, E. M., & Cohen, J. G. 1996, *AJ*, 112, 839
- Crain, R. A., Theuns, T., Dalla Vecchia, C., et al. 2009, *MNRAS*, 399, 1773
- Croton, D. J., Springel, V., White, S. D. M., et al. 2006, *MNRAS*, 365, 11

- Cucciati, O., Tresse, L., Ilbert, O., et al. 2012, *A&A*, 539, A31
- Daddi, E., Dickinson, M., Morrison, G., et al. 2007, *ApJ*, 670, 156
- Dalla Vecchia, C., Bower, R. G., Theuns, T., et al. 2004, *MNRAS*, 355, 995
- Dalla Vecchia, C., & Schaye, J. 2008, *MNRAS*, 387, 1431
- Davidzon, I., Bolzonella, M., Coupon, J., et al. 2013, *A&A*, 558, A23
- Davis, M., Efstathiou, G., Frenk, C. S., & White, S. D. M. 1985, *ApJ*, 292, 371
- Diemand, J., Kuhlen, M., Madau, P., et al. 2008, *Nature*, 454, 735
- Elbaz, D., Daddi, E., Le Borgne, D., et al. 2007, *A&A*, 468, 33
- Fabian, A. C., Sanders, J. S., Taylor, G. B., et al. 2006, *MNRAS*, 366, 417
- Fioc, M., & Rocca-Volmerange, B. 1997, *A&A*, 326, 950
- Fontana, A., Salimbeni, S., Grazian, A., et al. 2006, *A&A*, 459, 745
- Gallazzi, A., Charlot, S., Brinchmann, J., White, S. D. M., & Tremonti, C. A. 2005, *MNRAS*, 362, 41
- González, V., Labbé, I., Bouwens, R. J., et al. 2011, *ApJL*, 735, L34
- Governato, F., Brook, C., Mayer, L., et al. 2010, *Nature*, 463, 203
- Guedes, J., Callegari, S., Madau, P., & Mayer, L. 2011, *ApJ*, 742, 76
- Guo, Q., White, S., Li, C., & Boylan-Kolchin, M. 2010, *MNRAS*, 404, 1111
- Hopkins, A. M. 2004, *The Astrophysical Journal*, 615, 209
- Hopkins, P. F., Quataert, E., & Murray, N. 2011, *MNRAS*, 417, 950
- . 2012a, *MNRAS*, 421, 3522
- . 2012b, *MNRAS*, 421, 3488
- Ilbert, O., Salvato, M., Le Floc'h, E., et al. 2010, *ApJ*, 709, 644
- Inoue, A. K., Shimizu, I., Tamura, Y., et al. 2014, *ApJL*, 780, L18
- Kajisawa, M., Ichikawa, T., Yamada, T., et al. 2010, *ApJ*, 723, 129
- Kajisawa, M., Ichikawa, T., Tanaka, I., et al. 2009, *The Astrophysical Journal*, 702, 1393
- Kannan, R., Stinson, G. S., Macciò, A. V., et al. 2013, *MNRAS*, arXiv:1302.2618
- Karim, A., Schinnerer, E., Martínez-Sansigre, A., et al. 2011, *ApJ*, 730, 61
- Katz, N., Hernquist, L., & Weinberg, D. H. 1992, *ApJL*, 399, L109
- Kauffmann, G., White, S. D. M., & Guiderdoni, B. 1993, *MNRAS*, 264, 201
- Kawata, D., Okamoto, T., Gibson, B. K., Barnes, D. J., & Cen, R. 2013, *MNRAS*, 428, 1968
- Kennicutt, Jr., R. C. 1998, *ApJ*, 498, 541
- Kereš, D., Katz, N., Weinberg, D. H., & Davé, R. 2005, *MNRAS*, 363, 2
- Kewley, L. J., & Ellison, S. L. 2008, *ApJ*, 681, 1183
- Kobulnicky, H. A., & Kewley, L. J. 2004, *ApJ*, 617, 240
- Kroupa, P. 2001, *MNRAS*, 322, 231
- Li, C., & White, S. D. M. 2009, *MNRAS*, 398, 2177
- Maccarone, T. J., Gallo, E., & Fender, R. 2003, *MNRAS*, 345, L19
- Mannucci, F., Cresci, G., Maiolino, R., et al. 2009, *MNRAS*, 398, 1915
- Marigo, P. 2001, *A&A*, 370, 194
- Marinacci, F., Pakmor, R., & Springel, V. 2013, *MNRAS*, arXiv:1305.5360
- Martin, C. L. 2005, *ApJ*, 621, 227
- McGee, S. L., & Balogh, M. L. 2010, *MNRAS*, 403, L79
- Meier, D. L. 2001, *ApJL*, 548, L9
- Morris, J. P., & Monaghan, J. J. 1997, *Journal of Computational Physics*, 136, 41
- Moster, B. P., Naab, T., & White, S. D. M. 2013, *MNRAS*, 428, 3121
- Nagao, T., Maiolino, R., & Marconi, A. 2006, *A&A*, 459, 85
- Nagashima, M., Lacey, C. G., Baugh, C. M., Frenk, C. S., & Cole, S. 2005, *MNRAS*, 358, 1247
- Nagashima, M., Yahagi, H., Enoki, M., Yoshii, Y., & Gouda, N. 2005, *The Astrophysical Journal*, 634, 26
- Narayan, R. 2005, *Ap&SS*, 300, 177
- Narayan, R., Mahadevan, R., & Quataert, E. 1998, in *Theory of Black Hole Accretion Disks*, ed. M. A. Abramowicz, G. Björnsson, & J. E. Pringle, 148
- Noeske, K. G., Weiner, B. J., Faber, S. M., et al. 2007, *ApJL*, 660, L43
- Ocvirk, P., Pichon, C., & Teyssier, R. 2008, *MNRAS*, 390, 1326
- Okamoto, T. 2013, *MNRAS*, 428, 718
- Okamoto, T., Eke, V. R., Frenk, C. S., & Jenkins, A. 2005, *MNRAS*, 363, 1299
- Okamoto, T., Frenk, C. S., Jenkins, A., & Theuns, T. 2010, *MNRAS*, 406, 208
- Okamoto, T., Gao, L., & Theuns, T. 2008a, *MNRAS*, 390, 920
- Okamoto, T., Jenkins, A., Eke, V. R., Quilis, V., & Frenk, C. S. 2003, *MNRAS*, 345, 429
- Okamoto, T., & Nagashima, M. 2003, *ApJ*, 587, 500
- Okamoto, T., Nemmen, R. S., & Bower, R. G. 2008b, *MNRAS*, 385, 161
- Omma, H., Binney, J., Bryan, G., & Slyz, A. 2004, *MNRAS*, 348, 1105
- Oppenheimer, B. D., & Davé, R. 2006, *MNRAS*, 373, 1265
- . 2008, *MNRAS*, 387, 577
- Ouchi, M., Shimasaku, K., Okamura, S., et al. 2004, *ApJ*, 611, 660
- Parry, O. H., Eke, V. R., Frenk, C. S., & Okamoto, T. 2012, *MNRAS*, 419, 3304
- Pascale, E., Ade, P. A. R., Bock, J. J., et al. 2009, *ApJ*, 707, 1740
- Pettini, M., & Pagel, B. E. J. 2004, *MNRAS*, 348, L59
- Planck Collaboration. 2013, *ArXiv e-prints*, arXiv:1303.5076
- Portinari, L., Chiosi, C., & Bressan, A. 1998, *A&A*, 334, 505
- Price, D. J. 2008, *Journal of Computational Physics*, 2271, 10040
- Puchwein, E., & Springel, V. 2013, *MNRAS*, 428, 2966
- Quilis, V., Bower, R. G., & Balogh, M. L. 2001, *MNRAS*, 328, 1091
- Rees, M. J., Begelman, M. C., Blandford, R. D., & Phinney, E. S. 1982, *Nature*, 295, 17
- Rodighiero, G., Vaccari, M., Franceschini, A., et al. 2010, *A&A*, 515, A8
- Rosswog, S., & Price, D. 2007, *MNRAS*, 379, 915
- Saitoh, T. R., & Makino, J. 2009, *ApJL*, 697, L99
- Salpeter, E. E. 1955, *ApJ*, 121, 161
- Santini, P., Fontana, A., Grazian, A., et al. 2012, *A&A*, 538, A33
- Scannapieco, C., Wadepuhl, M., Parry, O. H., et al. 2012, *MNRAS*, 423, 1726
- Schaye, J., Dalla Vecchia, C., Booth, C. M., et al. 2010, *MNRAS*, 402, 1536

- Shakura, N. I., & Sunyaev, R. A. 1973, *A&A*, 24, 337
- Shen, S., Wadsley, J., & Stinson, G. 2010, *MNRAS*, 407, 1581
- Shimizu, I., Inoue, A. K., Okamoto, T., & Yoshida, N. 2013, ArXiv e-prints, arXiv:1310.0114
- Shimizu, I., Yoshida, N., & Okamoto, T. 2011, *MNRAS*, 418, 2273
- . 2012, ArXiv e-prints, 1207.3856
- Sijacki, D., & Springel, V. 2006, *MNRAS*, 366, 397
- Sijacki, D., Springel, V., Di Matteo, T., & Hernquist, L. 2007, *MNRAS*, 380, 877
- Somerville, R. S., & Primack, J. R. 1999, *MNRAS*, 310, 1087
- Springel, V. 2005, *MNRAS*, 364, 1105
- Springel, V., & Hernquist, L. 2003, *MNRAS*, 339, 289
- Springel, V., White, S. D. M., Tormen, G., & Kauffmann, G. 2001, *MNRAS*, 328, 726
- Springel, V., White, S. D. M., Jenkins, A., et al. 2005, *Nature*, 435, 629
- Springel, V., Wang, J., Vogelsberger, M., et al. 2008, *MNRAS*, 391, 1685
- Stinson, G., Seth, A., Katz, N., et al. 2006, *MNRAS*, 373, 1074
- Stinson, G. S., Brook, C., Macciò, A. V., et al. 2013, *MNRAS*, 428, 129
- Taylor, G. B., Sanders, J. S., Fabian, A. C., & Allen, S. W. 2006, *MNRAS*, 365, 705
- Teyssier, R., Pontzen, A., Dubois, Y., & Read, J. I. 2013, *MNRAS*, 429, 3068
- Thacker, R. J., & Couchman, H. M. P. 2001, *ApJL*, 555, L17
- Torrey, P., Vogelsberger, M., Genel, S., et al. 2013, ArXiv e-prints, arXiv:1305.4931
- Verma, A., Lehnert, M. D., Förster Schreiber, N. M., Bremer, M. N., & Douglas, L. 2007, *MNRAS*, 377, 1024
- Vogelsberger, M., Genel, S., Sijacki, D., et al. 2013, *MNRAS*, 436, 3031
- Weinberg, D. H., Hernquist, L., & Katz, N. 1997, *ApJ*, 477, 8
- White, S. D. M., & Frenk, C. S. 1991, *ApJ*, 379, 52
- Wiersma, R. P. C., Schaye, J., & Smith, B. D. 2009a, *MNRAS*, 393, 99
- Wiersma, R. P. C., Schaye, J., Theuns, T., Dalla Vecchia, C., & Tornatore, L. 2009b, *MNRAS*, 399, 574
- Wise, J. H., Abel, T., Turk, M. J., Norman, M. L., & Smith, B. D. 2012, *MNRAS*, 427, 311
- Yabe, K., Ohta, K., Iwamuro, F., et al. 2014, *MNRAS*, 437, 3647
- Zahid, H. J., Dima, G. I., Kewley, L. J., Erb, D. K., & Davé, R. 2012, *ApJ*, 757, 54
- Zahid, H. J., Kashino, D., Silverman, J. D., et al. 2013, ArXiv e-prints, arXiv:1310.4950
- Zibetti, S., White, S. D. M., Schneider, D. P., & Brinkmann, J. 2005, *MNRAS*, 358, 949